

**Ultrafast Photo-driven Charge Transfer Exciton Dynamics in
Mixed-Stack Pyrene-Perylenediimide Single Cococrystals**

Journal:	<i>Journal of Materials Chemistry C</i>
Manuscript ID	TC-COM-09-2021-004313.R1
Article Type:	Communication
Date Submitted by the Author:	23-Oct-2021
Complete List of Authors:	Myong, Michele; Northwestern University, Department of Chemistry Qi, Yue; Northwestern University, Department of Chemistry Stern, Charlotte; Northwestern University, Chemistry Wasielewski, Michael; Northwestern University, Department of Chemistry

Ultrafast Photo-driven Charge Transfer Exciton Dynamics in Mixed-Stack Pyrene-Perylenediimide Single Co-crystals

Michele S. Myong, Yue Qi, Charlotte Stern, and Michael R. Wasielewski*

ABSTRACT

Electron donor-acceptor co-crystals are receiving increasing interest because of their many useful optoelectronic properties. While the steady-state properties of many different co-crystals have been characterized, very few studies have addressed how crystal morphology affects the dynamics of charge transfer (CT) exciton formation, migration, and decay, which are often critical to their performance in device structures. Here we show that co-crystallization of a pyrene (Pyr) electron donor with either *N,N'*-bis(2,6-diisopropylphenyl)- or *N,N'*-bis(3'-pentyl)-perylene-3,4:9,10-bis(dicarboximide) (diisoPDI or C₅PDI) electron acceptors, respectively, yields mixed π -stacked Pyr-diisoPDI or Pyr-C₅PDI donor-acceptor co-crystals. Femtosecond transient absorption microscopy is used to determine the CT exciton dynamics in these single crystals. Fitting the data to a one-dimensional charge transfer CT exciton diffusion model reveals a diffusion constant that is two orders of magnitude higher in the Pyr-diisoPDI co-crystal compared to the Pyr-C₅PDI co-crystal. By correlating the co-crystal structures to their distinct excited-state dynamics, the effects of each mixed stacked structure on the exciton dynamics and the mechanisms of CT exciton diffusion are elucidated.

Department of Chemistry and Institute for Sustainability and Energy at Northwestern, Northwestern University, 2145 Sheridan Road, Evanston, Illinois 60208-3113

Email: m-wasielewski@northwestern.edu

† Electronic supplementary information (ESI) available: description of crystal growth and structure determination, steady-state absorption and emission microscopy, femtosecond transient absorption microscopy, calculation of excitation density, calculation of diffusion coefficients.

INTRODUCTION

Organic donor-acceptor (D-A) co-crystals are formed by charge transfer (CT) interactions between their two components, which result in new photophysical properties¹⁻³ with potential applications in tunable dye lasers,^{4, 5} sensors,^{6, 7} and organic photovoltaics.⁸⁻¹¹ Several studies characterizing the CT ground state optical absorption as well as the steady-state and time-resolved photoluminescence of D-A co-crystals have been reported.^{2, 12-23} While a few reports on excited state dynamics in D-A co-crystals employ transient absorption and emission spectroscopy on polycrystalline powders to draw conclusions about the crystal morphology dependence of the dynamics,^{14, 24-27} there are even fewer studies that employ transient optical absorption measurements to study CT exciton dynamics in single D-A co-crystals.²⁸⁻³⁰

Port and co-workers reported the first example of using femtosecond transient absorption to study ultrafast CT exciton dynamics in single co-crystals of anthracene and pyromellitic dianhydride.^{28, 29} We recently reported on a single co-crystal of a *peri*-xanthenoxanthene (PXX) donor with a *N,N'*-bis(3'-pentyl)-2,5,8,11-tetraphenylperylene-3,4:9,10-bis(dicarboximide) (Ph₄PDI) acceptor to give an orthorhombic PXX-Ph₄PDI D-A π -stacked co-crystal with a CT transition dipole moment (TDM) perpendicular to the TDMs for S_n ← S₀ excitation of PXX and Ph₄PDI. Using polarized, broadband, femtosecond transient absorption microscopy (fsTAM), we determined that selective photoexcitation of Ph₄PDI in the single co-crystal results in CT exciton formation within the 300-fs instrument response time. At early times ($0.3 \leq t \leq 500$ ps), the CT excitons decay with a $t^{-1/2}$ dependence, which was attributed to CT biexciton annihilation within the one-dimensional D-A π -stacks producing high-energy, long-lived (>8 ns) electron-hole pairs in the crystal.

Here, we have co-crystallized a pyrene (Pyr) electron donor with either an *N,N'*-bis(2,6-diisopropylphenyl)- or *N,N'*-bis(3'-pentyl)-perylene-3,4:9,10-bis(dicarboximide) (diisoPDI or C₅PDI) electron acceptor to yield single Pyr-diisoPDI or Pyr-C₅PDI donor-acceptor co-crystals with mixed π -stacking. Polarized, broadband fsTAM was used to study the CT exciton dynamics of Pyr-diisoPDI and Pyr-C₅PDI single co-crystals, which reveal that the CT exciton diffusion coefficient in the Pyr-diisoPDI co-crystal ($\sim 1 \times 10^{-4}$ cm²/s) is about two orders of magnitude higher than that of Pyr-C₅PDI ($\sim 6 \times 10^{-6}$ cm²/s). Additionally, when the pump polarization is perpendicular to its crystallographic *a*-axis (crystal long axis), the CT exciton decay kinetics in the Pyr-diisoPDI co-crystal are dominated by CT exciton annihilation, while charge recombination of the CT exciton contributes significantly to the dynamics when the pump polarization is parallel to the *a*-axis. In contrast, CT exciton recombination contributes significantly to the dynamics in the Pyr-C₅PDI co-crystal for both pump polarizations. A comparison of the two co-crystal morphologies shows that CT exciton diffusion is most likely confined to individual D-A π stacks in the Pyr-C₅PDI co-crystal, while rapid charge hopping or delocalization between adjacent donors and acceptors in the Pyr-diisoPDI co-crystal results in more rapid diffusion, even though CT exciton diffusion remains one-dimensional. These results provide insight into how crystal morphologies can be designed to tailor CT exciton mobilities in organic semiconductors for optoelectronic applications.

RESULTS AND DISCUSSION

Donor-acceptor co-crystal structures

Single co-crystals containing a 1:1 stoichiometric ratio of pyrene to either diisoPDI or C₅PDI in their unit cells were grown and their x-ray diffraction structures were determined using techniques given in the ESI. The Pyr-diisoPDI co-crystal is monoclinic with the space group P2₁/c.

Bravais-Friedel-Donnay-Harker (BFDH) cell morphology calculations (Figures S1) show that the crystallographic a -axis is nearly parallel to the crystal long axis. The view down the b - c

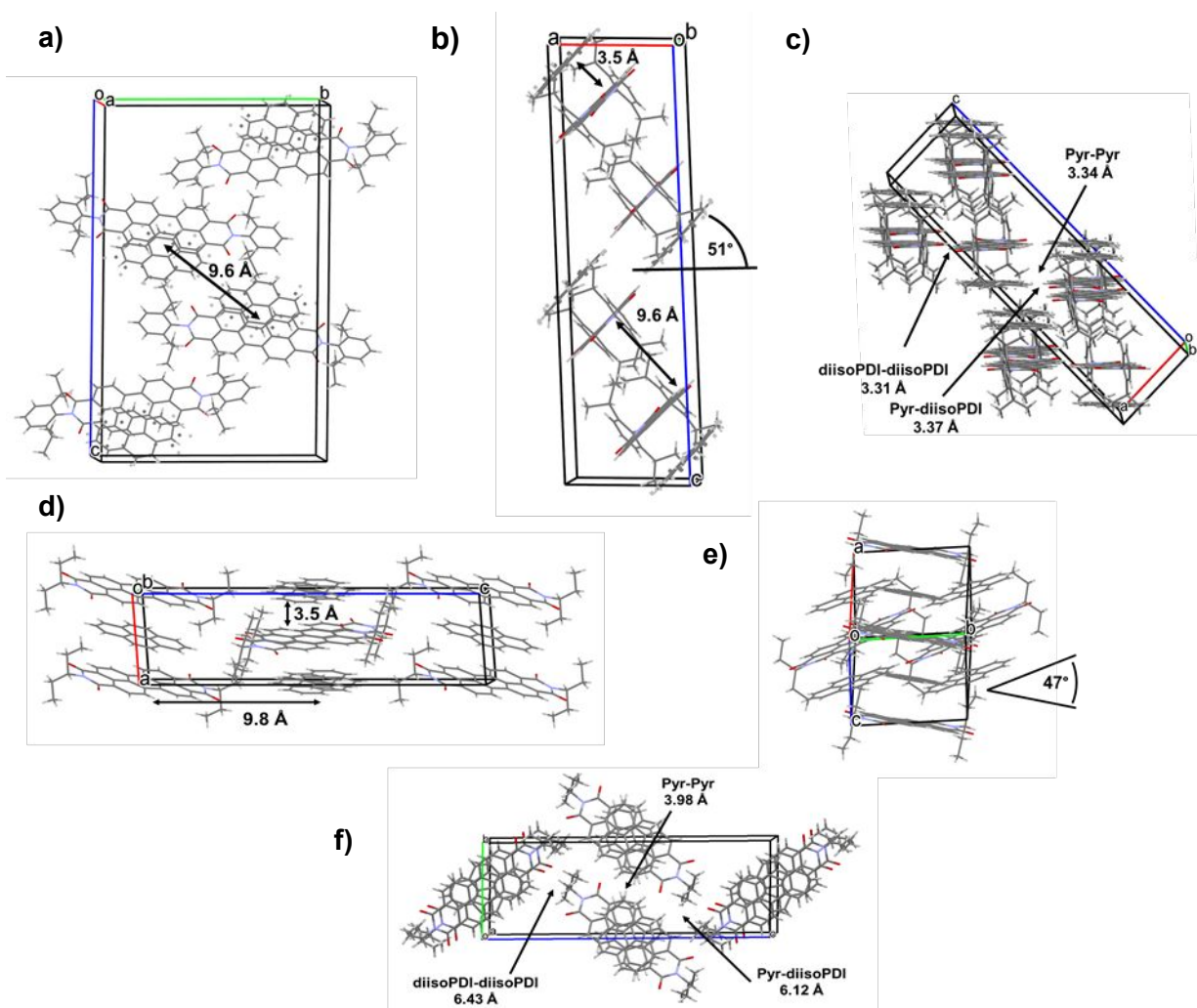


Figure 1. Pyr-diisoPDI cocrystal structure: (a) View down the b - c crystallographic plane with the interstack distance labeled, (b) View down the a - c crystallographic plane with the Pyr-diisoPDI and diisoPDI-diisoPDI distances labeled as well as the angle between the planes of the molecules and the crystallographic c -axis, and (c) View nearly in line with the crystallographic b -axis showing the edge-to-edge π - π distances of Pyr-Pyr, Pyr-diisoPDI, and diisoPDI-diisoPDI. Pyr- C_5 PDI cocrystal structure: (d) View down the a - c crystallographic plane with intrastack and interstack distances labeled, (e) View down the a - b crystallographic plane, (f) View down the crystallographic a -axis with the Pyr- C_5 PDI, C_5 PDI- C_5 PDI, and Pyr-Pyr distances labeled.

crystallographic plane shows that the interstack distance between the D-A pairs is 9.6 Å (Figure 1a). The planes of the diisoPDI and pyrene molecules are tilted 51° from the a -axis of the unit cell (Figure 1b) and the Pyr-diisoPDI π - π stacking distance is 3.5 Å. While the center-to-center distance

between two diisoPDI molecules in separate D-A stacks is 7.2 Å, they have an edge-to-edge distance of one of their oxygen atoms to the carbon atom of an adjacent diisoPDI of only 3.31 Å (Figure 1c). The structure also shows that half of the Pyr molecules are in the same plane as diisoPDI with an edge-to-edge closest distance of the diisoPDI oxygen atom to the Pyr carbon atom of 3.37 Å. In addition, adjacent Pyr molecules have a slip-stacked arrangement in which the closest edge-to-edge distance of their π systems is only 3.34 Å. While the intrastack π - π interactions of the cofacial Pyr and diisoPDI should be large, given the close edge-to-edge interstack Pyr-Pyr, diisoPDI- diisoPDI, and Pyr-diisoPDI distances (Figure 1c), the interstack electronic interactions may also be sufficiently large to influence the formation, migration, and decay of CT excitons.

The Pyr-C₅PDI co-crystal is triclinic with space group P-1 and its interstack distance is 9.8 Å, while the Pyr-C₅PDI π - π stacking distance is 3.5 Å, both of which are very similar to the Pyr-diisoPDI co-crystal (Figure 1d). BFDH cell morphology calculations (Figure S2) once again show that the crystallographic *a*-axis is nearly parallel to the crystal long axis. Looking down at the *a*-*b* crystallographic plane, the angle between the planes of adjacent D-A stacks is 47° (Figure 1e). In contrast to the Pyr-diisoPDI co-crystal, the Pyr-C₅PDI co-crystal has significantly greater edge-to-edge π - π distances of closest approach, where these distances are 6.43 Å for C₅PDI-C₅PDI, 6.12 Å for Pyr-C₅PDI, and 3.98 Å for Pyr-Pyr (Figure 1f). This implies that the photophysics of the Pyr-C₅PDI may be dominated by intrastack cofacial D-A interactions.

Steady-state absorption and emission microscopy

Polarization-dependent steady-state absorption and PL spectra of both co-crystals are shown in Figure 2. The Pyr-diisoPDI co-crystal exhibits three distinct absorption bands at 460, 510, and 550 nm that are assigned to transitions of diisoPDI (Figure 2a).³⁰ Absorption peaks related only to

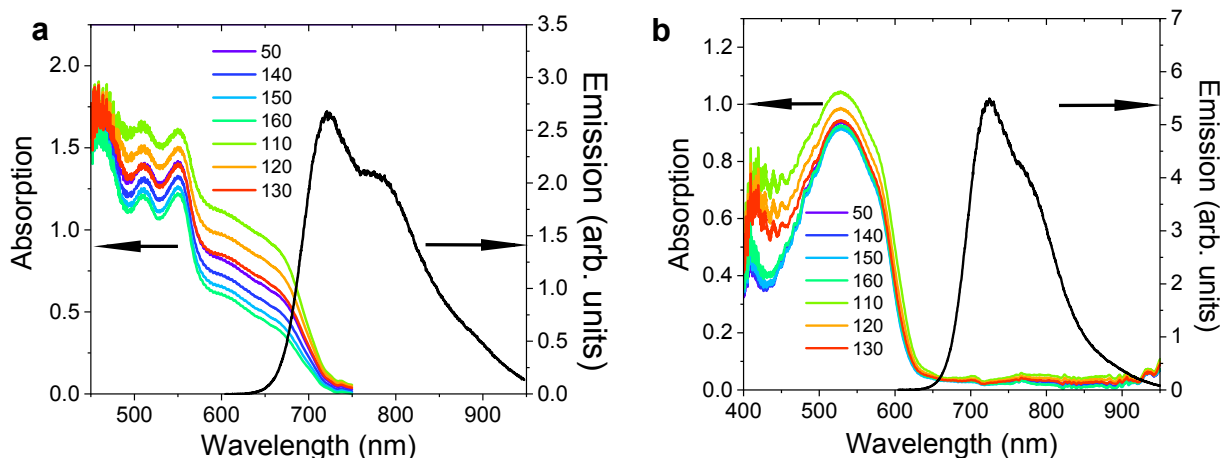


Figure 2. Steady-state absorption spectra at various polarizations with respect to the macroscopic crystal long axis (crystallographic a -axis), and unpolarized PL of (a) Pyr-diisoPDI cocrystal and (b) Pyr- C_5 PDI cocrystal.

Pyr are not observed because the molecule absorbs at 300-350 nm, which is outside of the range of the absorption measurement. The absorption in the 600-700 nm range is assigned to the CT band of the co-crystal.³⁰ The CT TDM lies along the direction normal to the π -stacking direction, so that the TDM makes an angle of $\sim 40^\circ$ relative to the crystallographic a -axis, which is parallel to the glass substrate surface. In contrast, the TDM of diisoPDI lies along its N-N axis,³¹ which is also $\sim 40^\circ$ relative to the crystallographic a -axis. As the direction of the linearly polarized light relative to the a -axis is changed, both the diisoPDI and CT bands exhibit modest intensity changes (Figure 2a). Additional polarized absorption data are given in Figure S3. The unpolarized PL spectrum of the Pyr-diisoPDI co-crystal shows a maximum at 710 nm.

The Pyr- C_5 PDI co-crystal displays a broad absorption band with a maximum at 530 nm and a shoulder at 577 nm that are both assigned to vibronic transitions of C_5 PDI (Figure 2b).³¹ The Pyr- C_5 PDI CT band is not observed because its TDM is nearly perpendicular to the crystallographic a -axis, which is parallel to the glass substrate surface, and is thus nearly orthogonal to all orientations of the polarized light.³⁰ The orientation of the C_5 PDI TDM³¹ is $\sim 40^\circ$ relative to the crystallographic a -axis, so that the C_5 PDI absorption of the co-crystal exhibits a modest

dependence of the polarized light orientation. The sharp absorption band at 410 nm may result from the red-shifted pyrene absorption in the solid state. Additional polarized absorption data are given in Figure S4. The unpolarized PL spectrum of the Pyr-C₅PDI single crystal shows a band maximum at 710 nm, which is nearly identical to that of Pyr-diisoPDI. We assign this PL to the CT emission in both co-crystals.

Femtosecond transient absorption microscopy

Polarization-dependent femtosecond transient absorption microscopy (fsTAM) was used to investigate the CT exciton dynamics of both the Pyr-diisoPDI and Pyr-C₅PDI co-crystals. The pump and probe focused spot sizes (FWHM) on the sample were 0.83 μm and 0.93 μm , with Gaussian beam shapes (Figure S5). The total instrument response function (IRF) was 300 fs. The spectral features of Pyr-diisoPDI differ when the probe polarization is parallel or perpendicular to the *a*-axis of the co-crystal. After selective photoexcitation of diisoPDI at 540 nm, an absorption peak appears at 710 nm within the IRF when the probe is perpendicular to the crystallographic *a*-axis that is assigned to diisoPDI^{•-} within the Pyr^{•+}-diisoPDI^{•-} exciton (Figure 3a).³² In contrast, when the probe direction is parallel to the crystal *a*-axis, the diisoPDI^{•-} positive absorption feature broadens. Both spectra decay over the ~ 8 ns time window of the pump-probe experiment. The spectral shape resembles the solution phase spectrum of PDI^{•-} observed previously.³² Pyr^{•+} is not observed because the spectral feature would be around 400 nm,³³ which is outside the wavelength window of the experiment. The sharper diisoPDI^{•-} absorption observed for the perpendicular probe orientation is a consequence of cancellation of part of the diisoPDI^{•-} absorption by the ground state bleach of the CT absorption band at 600-700nm (Figure 3a). When the probe is parallel to the crystallographic *a*-axis, the ground state bleach of the CT band is diminished and thus, the diisoPDI^{•-} absorption appears more symmetric (Figure 3b).

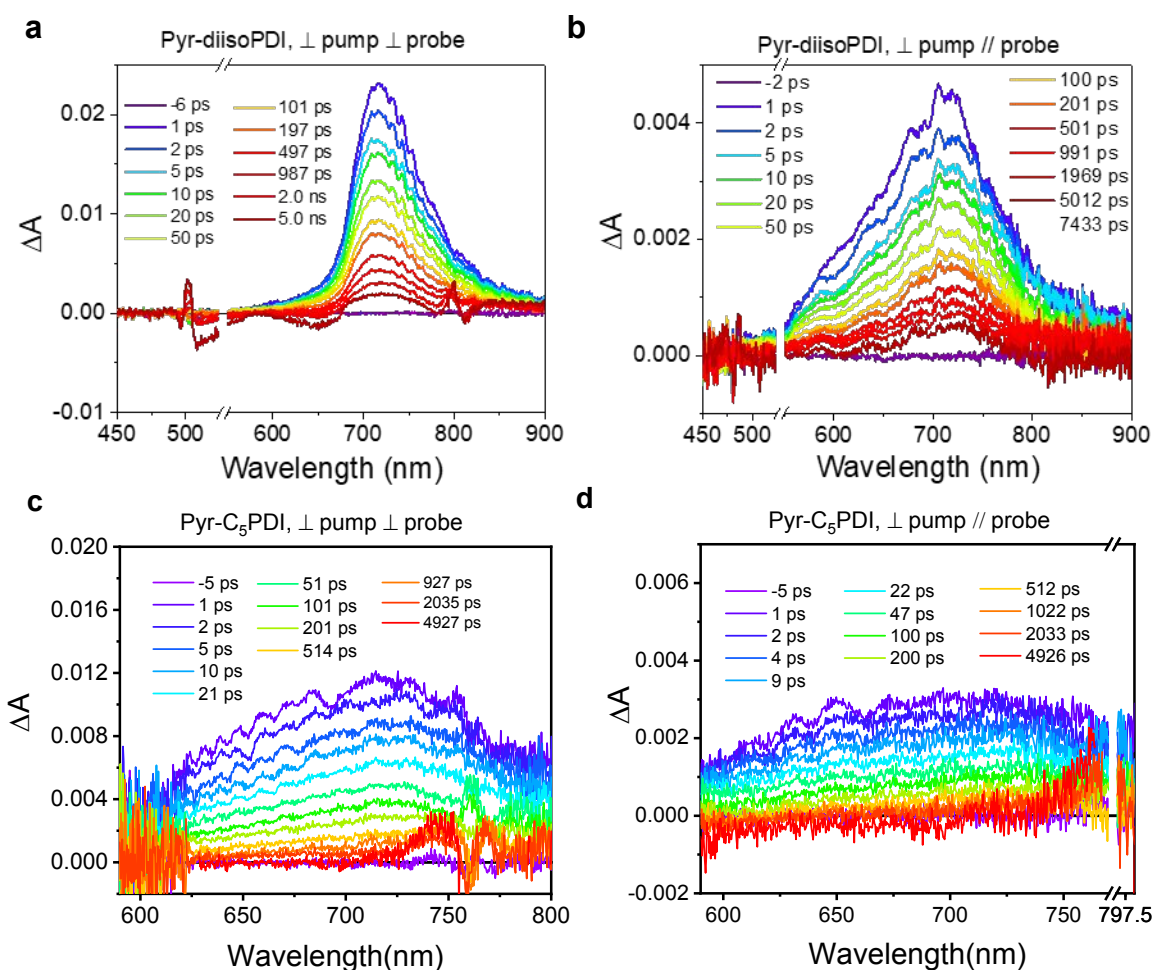


Figure 3. fsTAM spectra of the Pyr-diisoPDI cocrystal with probe polarized (a) perpendicular or (b) parallel to crystallographic *a*-axis and of the Pyr-C₅PDI cocrystal with probe polarized (c) perpendicular or (d) parallel to crystallographic *a*-axis. The excitation power density for all spectra was $3.0 \times 10^{20} \text{ cm}^{-3}$.

The fsTAM spectra of the Pyr-C₅PDI co-crystal are only slightly probe-polarization dependent. After selective excitation of C₅PDI, formation of the Pyr^{•+}-C₅PDI^{•-} CT exciton is observed as a broadened positive absorption band at 700 nm due to C₅PDI^{•-} when the probe is perpendicular to the *a*-axis of the crystal. The C₅PDI^{•-} feature decays within the 8 ns pump-probe delay window (Figure 3c). Similar somewhat broader spectral features are observed when the probe is parallel to the crystal long axis. C₅PDI^{•-} is observed at 700 nm along with a shoulder at 640 nm (Figure 3d).

CT exciton diffusion and decay dynamics

Our data show that the kinetics of CT exciton diffusion in the Pyr-diisoPDI co-crystal depend on the pump polarization relative to the crystallographic a -axis. When the pump is polarized perpendicular to the crystallographic a -axis, the TDM of diisoPDI within the Pyr-diisoPDI co-crystal is nearly parallel to the polarization direction of the light (Figure 1a), so maximal light absorption occurs. The decay kinetics are best modeled using a bimolecular, one-dimensional CT exciton annihilation process:

$$\frac{d[\text{CT}]}{dt} = -k_2[\text{CT}]^2 \quad (1)$$

which for a Smoluchowski-type time-dependent rate coefficient $k_2 \propto t^{-1/2}$ has the analytical solution:³⁴

$$[\text{CT}] = ([\text{CT}]_0^{-1} + 2C\sqrt{t})^{-1} \quad (2)$$

where C is a composite constant discussed below. This model fits the data well for the ~ 8 ns time window of the pump-probe experiment (Figure 4a).

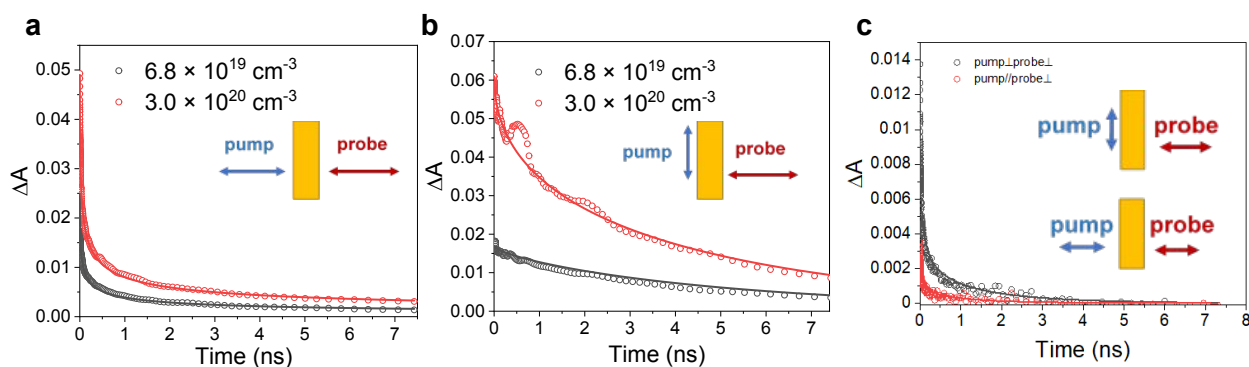


Figure 4. (a) Kinetic fits at 710 nm to a bimolecular, one-dimensional decay model at two different pump fluences for Pyr-diisoPDI with the indicated pump and probe polarizations. (b) Kinetic fits to a bimolecular, one-dimensional decay and first order decay model at two different pump fluences for the Pyr-diisoPDI cocrystal with the indicated pump and probe polarizations. Oscillations in the data are due to acoustic phonons produced in the cocrystal at higher pump powers. (c) Kinetic fits to a bimolecular, one-dimensional decay and first order decay model in the Pyr-C₅PDI cocrystal at 710 nm with the indicated pump and probe polarizations. The excitation density is $6.8 \times 10^{19} \text{ cm}^{-3}$ for both polarizations. Oscillations in the data are due to acoustic phonons produced in the cocrystal at higher pump powers.

In contrast, when the pump is polarized parallel to the crystallographic *a*-axis, the TDM of diisoPDI within the Pyr-diisoPDI co-crystal is nearly perpendicular to the polarization direction of the pump diminishing the absorbance. The kinetic model that best describes the data requires the addition of a first order decay component to eqn. 1:

$$\frac{d[\text{CT}]}{dt} = -k_1[\text{CT}] - k_2[\text{CT}]^2 \quad (3)$$

The analytical solution³⁵ to eqn. 3 as detailed in the ESI is:

$$[\text{CT}] = \frac{[\text{CT}]_0 \sqrt{k_1} e^{-k_1 t}}{\sqrt{k_1} + [\text{CT}]_0 C \sqrt{\pi} - [\text{CT}]_0 C \sqrt{\pi} \times \text{erfc}(\sqrt{k_1 t})} \quad (4)$$

This model fits the data well for the ~8 ns time window of the pump-probe experiment (Figure 4b).

Charge recombination of the CT exciton begins to compete with the CT biexciton annihilation process when the pump polarization changes because irradiating the crystal with a parallel polarized pump reduces the number of absorbed photons and leads to fewer initial CT excitons produced (Figure 4b). This leads to a diminished CT biexciton annihilation rate and increased contribution of charge recombination to the decay kinetics. Indeed, the effects of the concentration of CT excitons on the kinetics can be seen in both pump polarizations when the incident pump power is decreased from 17 μW to 3.8 μW (Figures 4a and 4b). The lower concentration of CT excitons causes the nonlinear contribution in eqn. 3 to diminish, leading to slower decay kinetics and a larger contribution of first-order geminate charge recombination.

The TDM of C₅PDI in the Pyr-C₅PDI co-crystal is rotated by ~40° relative to the crystallographic *a*-axis, so that the CT exciton dynamics are nearly independent of the pump polarization direction. The CT exciton dynamics in the Pyr-C₅PDI co-crystal are best modeled using eqns. 3 and 4, regardless of pump polarization direction. The Pyr-C₅PDI transient absorption

data and kinetic fits using eqn. 4 are shown in Figure 4c. The presence of a significant first-order decay term at both pump polarizations indicates there is a significant contribution from the CT exciton recombination in addition to the dominant CT biexciton annihilation process. This is reasonable because interstack CT exciton diffusion is strongly diminished by the long C₅PDI-C₅PDI and Pyr-Pyr edge-to-edge distances (Figure 1f), relative to the corresponding distances in the Pyr-diisoPDI co-crystal (see below).

The bimolecular annihilation rate constant, k_2 , can be cast as a one-dimensional diffusion coefficient using:³⁵

$$k_2 = \frac{1}{R_{1D}N_0\sqrt{\frac{8D_{1D}}{\pi t}}} = \frac{C}{\sqrt{t}} \quad (5)$$

where R_{1D} is the annihilation radius in one-dimension and is approximated by the distance between the D-A pairs in the co-crystal structures. The R_{1D} values for Pyr-diisoPDI and Pyr-C₅PDI are 1.06×10^{-7} cm and 1.20×10^{-7} cm, respectively. N_0 is the average molecular density of the system (see Eq. 3, ESI, page S-3). Using the value of C in eqn. 5, we calculated the CT exciton diffusion coefficients for both Pyr-diisoPDI and Pyr-C₅PDI, which are listed in Table 1. The details of the calculations for the diffusion coefficients from C and ΔA are given in the ESI (eqns. S1-S12). While the mobility of the CT exciton in a donor-acceptor co-crystal can be described by a hopping rate,³⁰ the movement of excitons in crystalline pentacene and similar materials has also been modeled by a diffusion coefficient.³⁵⁻³⁸ It is known that CT excitons in mixed-stack donor-acceptor systems diffuse via a superexchange mechanism, where the hole on D⁺ tunnels to the next D through a virtual singlet state, ¹*A.^{30, 39-43} A similar mechanism for tunneling of A⁻ is possible, but less likely in the cases presented here because the virtual ¹*D is much higher in energy.

Table 1: Rate constants, C values, and diffusion coefficients for Pyr-diisoPDI and Pyr-C₅PDI cocrystals at different pump polarizations.

Co-crystal	k_1 (ps ⁻¹)	C (cm ³ ·s ^{-1/2})	D (cm ² /s)
Pyr-diisoPDI, ⊥ pump	-- ^a	5.64×10^{-16}	1.00×10^{-4}
Pyr-diisoPDI, pump	$1.57 \pm 0.08 \times 10^{-4}$	1.35×10^{-17}	5.75×10^{-8}
Pyr-C ₅ PDI, ⊥ pump	$5.1 \pm 0.3 \times 10^{-4}$	1.72×10^{-16}	5.65×10^{-6}
Pyr-C ₅ PDI, pump	$6.3 \pm 0.5 \times 10^{-4}$	1.67×10^{-16}	5.37×10^{-6}

^a The Pyr-diisoPDI cocrystal with the pump perpendicularly polarized to its crystallographic *a*-axis is fit to the kinetic model shown in Eq. 1. The other cocrystal data are fit to the kinetic model in Eq. 3.

What aspect of the Pyr-diisoPDI co-crystal structure leads to a 100-fold increase in its CT exciton diffusion coefficient relative to that of the Pyr-C₅PDI co-crystal? Photoexciting the Pyr-diisoPDI co-crystal may lead to efficient charge hopping or delocalization because the diisoPDI-diisoPDI and Pyr-Pyr edge-to-edge distances are close enough to ensure interstack wavefunction overlap (Figure 1c). Using EPR and ENDOR spectroscopy, we demonstrated earlier that the radical anions of PDI dimers and trimers with orthogonal core π -systems separated by ~ 3.2 Å have charge hopping rates that are $\gg 10^7$ s⁻¹,⁴⁴ so that the nearly coplanar diisoPDI π -systems in the Pyr-diisoPDI co-crystal should also have a comparable or higher hopping rate. Dispersing the charge in the CT exciton will reduce the Coulomb attraction of the CT state and the probability of charge recombination.⁴⁵ Moreover, charge dispersal should result in additional electronic coupling pathways for CT exciton diffusion via the superexchange mechanism outlined above. Thus, CT exciton diffusion becomes more favorable, even though CT exciton migration remains largely one-dimensional. When the Pyr-diisoPDI co-crystal is excited with the pump polarized parallel to the crystallographic *a*-axis, the diisoPDI TDM is perpendicular to the pump polarization, which results in far fewer CT excitons produced. The significantly lower diffusion coefficient of $\sim 6 \times 10^{-8}$ cm²/s

observed for this situation is most likely a consequence CT excitons produced at defect sites within the crystal having diisoPDI TDM orientations that favor CT exciton formation, but geometries that do not favor CT exciton diffusion. In contrast, the Pyr-C₅PDI cofacial π -stacks in the co-crystal structure are positioned farther apart, so that charge hopping or delocalization between adjacent π -stacks is unlikely, thus confining CT exciton diffusion to the individual π -stacks. Therefore, the fact that the CT exciton diffusion coefficient for the Pyr-diisoPDI co-crystal is much larger than that of the Pyr-C₅PDI co-crystal is consistent with the co-crystal morphologies, although one cannot completely discount some contribution from differences in the density of CT exciton trap sites.

CONCLUSIONS

Two co-crystals, Pyr-diisoPDI and Pyr-C₅PDI, were characterized using X-ray crystallography, steady-state absorption and emission microscopy and fsTAM. The fsTAM spectra of both co-crystals indicates the formation of Pyr^{•+}-diisoPDI^{•-} and Pyr^{•+}-C₅PDI^{•-} CT excitons, whose kinetics were modeled using a one-dimensional CT exciton annihilation model with the addition of a first-order decay term in certain cases. It was determined that one-dimensional CT exciton diffusion occurs in the π -stacking direction in both Pyr-diisoPDI and Pyr-C₅PDI co-crystals. The 100-fold increase in the CT exciton diffusion coefficient of the Pyr-diisoPDI co-crystal relative to that of the Pyr-C₅PDI co-crystal is attributed to charge dispersal within the CT exciton in the former case. These results illustrate how D-A co-crystal morphology strongly influences CT exciton diffusion and provide insight into optimizing D-A-co-crystals for optoelectronic applications.

Conflicts of Interest

There are no conflicts to declare.

ACKNOWLEDGMENTS

This work was supported by the National Science Foundation under Award DMR-2003739. Use was made of the IMSERC X-ray Facility at Northwestern University, which has received support from the Soft and Hybrid Nanotechnology Experimental (SHyNE) Resource (NSF ECCS-1542205) and Northwestern University.

NOTES AND REFERENCES

1. W. Zhu, L. Zhu, Y. Zou, Y. Wu, Y. Zhen, H. Dong, H. Fu, Z. Wei, Q. Shi and W. Hu, *Adv. Mater.*, 2016, **28**, 5954-5962.
2. M. Wykes, S. K. Park, S. Bhattacharyya, S. Varghese, J. E. Kwon, D. R. Whang, I. Cho, R. Wannemacher, L. Luer, S. Y. Park and J. Gierschner, *J. Phys. Chem. Lett.*, 2015, **6**, 3682-3687.
3. M. Kumar, K. Venkata Rao and S. J. George, *Phys. Chem. Chem. Phys.*, 2014, **16**, 1300-1313.
4. C. L. Chiang, S. M. Tseng, C. T. Chen, C. P. Hsu and C. F. Shu, *Adv. Funct. Mater.*, 2008, **18**, 248-257.
5. H. Wang, F. Li, B. Gao, Z. Xie, S. Liu, C. Wang, D. Hu, F. Shen, Y. Xu, H. Shang, Q. Chen, Y. Ma and H. Sun, *Cryst. Growth Des.*, 2009, **9**, 4945-4950.
6. L. Zang, Y. Che and J. S. Moore, *Acc. Chem. Res.*, 2008, **41**, 1596-1608.
7. Z. Ning, Z. Chen, Q. Zhang, Y. Yan, S. Qian, Y. Cao and H. Tian, *Adv. Funct. Mater.*, 2007, **17**, 3799-3807.
8. R. H. Friend, R. W. Gymer, A. B. Holmes, J. H. Burroughes, R. N. Marks, C. Taliani, D. D. C. Bradley, D. A. D. Santos, J. L. Brédas, M. Lögdlund and W. R. Salaneck, *Nature*, 1999, **397**, 121-128.

9. J. H. Lee, Y. Y. Yuan, Y. J. Kang, W. L. Jia, Z. H. Lu and S. N. Wang, *Adv. Funct. Mater.*, 2006, **16**, 681-686.
10. N. J. Tremblay, A. A. Gorodetsky, M. P. Cox, T. Schiros, B. Kim, R. Steiner, Z. Bullard, A. Sattler, W.-Y. So, Y. Itoh, M. F. Toney, H. Ogasawara, A. P. Ramirez, I. Kymissis, M. L. Steigerwald and C. Nuckolls, *ChemPhysChem*, 2010, **11**, 799-803.
11. S. J. Kang, S. Ahn, J. B. Kim, C. Schenck, A. M. Hiszpanski, S. Oh, T. Schiros, Y.-L. Loo and C. Nuckolls, *J. Am. Chem. Soc.*, 2013, **135**, 2207-2212.
12. S. K. Park, S. Varghese, J. H. Kim, S. J. Yoon, O. K. Kwon, B. K. An, J. Gierschner and S. Y. Park, *J. Am. Chem. Soc.*, 2013, **135**, 4757-4764.
13. Y. Q. Sun, Y. L. Lei, X. H. Sun, S. T. Lee and L. S. Liao, *Chem. Mater.*, 2015, **27**, 1157-1163.
14. C. Wang, J. Wang, N. Wu, M. Xu, X. Yang, Y. Lu and L. Zang, *RSC Advances*, 2017, **7**, 2382-2387.
15. W. G. Zhu, L. Y. Zhu, Y. Zou, Y. S. Wu, Y. G. Zhen, H. L. Dong, H. B. Fu, Z. X. Wei, Q. Shi and W. P. Hu, *Adv. Mater.*, 2016, **28**, 7563-7563.
16. W. G. Zhu, R. H. Zheng, X. L. Fu, H. B. Fu, Q. Shi, Y. G. Zhen, H. L. Dong and W. P. Hu, *Angew. Chem., Int. Ed.*, 2015, **54**, 6785-6789.
17. H. Geng, X. Y. Zheng, Z. G. Shuai, L. Y. Zhu and Y. P. Yi, *Adv. Mater.*, 2015, **27**, 1443-1449.
18. Y. Wan, Z. Guo, T. Zhu, S. Yan, J. Johnson and L. Huang, *Nat. Chem.*, 2015, **7**, 785-792.
19. T. Zhu, Y. Wan, Z. Guo, J. Johnson and L. Huang, *Adv. Mater.*, 2016, **28**, 7939-7947.
20. B. D. Folie, J. B. Haber, S. Refaely-Abramson, J. B. Neaton and N. S. Ginsberg, *J. Am. Chem. Soc.*, 2018, **140**, 2326-2335.

21. Y. Dong, B. Xu, J. Zhang, X. Tan, L. Wang, J. Chen, H. Lv, S. Wen, B. Li, L. Ye, B. Zou and W. Tian, *Angew. Chem. Int. Ed.*, 2012, **51**, 10782-10785.
22. D. Yan and D. G. Evans, *Mater. Horiz.*, 2014, **1**, 46-57.
23. Z. Ding, H. Shang, S. Zhang, W. Han, B. Li and S. Jiang, *Cryst. Growth Des.*, 2020, **20**, 5203-5210.
24. D. Sun, G.-H. Deng, B. Xu, E. Xu, X. Li, Y. Wu, Y. Qian, Y. Zhong, C. Nuckolls, A. R. Harutyunyan, H.-L. Dai, G. Chen, H. Chen and Y. Rao, *iScience*, 2019, **19**, 1079-1089.
25. R. J. Dillon and C. J. Bardeen, *J. Phys. Chem. A*, 2011, **115**, 1627-1633.
26. R. J. Dillon and C. J. Bardeen, *J. Phys. Chem. A*, 2012, **116**, 5145-5150.
27. S. Sun, J. Pang, S. Ni, G. Zhang, L. Xu, L. Dang and M.-D. Li, *J. Phys. Chem. C*, 2020, **124**, 17744–17751.
28. A. Hartschuh, H. Port and H. C. Wolf, *J. Lumin.*, 2001, **94&95**, 441-445.
29. H. Port and A. Hartschuh, *J. Lumin.*, 2004, **110**, 315-324.
30. I. Schlesinger, N. E. Powers-Riggs, J. L. Logsdon, Y. Qi, S. A. Miller, R. Tempelaar, R. M. Young and M. R. Wasielewski, *Chem. Sci.*, 2020, **11**, 9532-9541.
31. F. Würthner, C. R. Saha-Möller, B. Fimmel, S. Ogi, P. Leowanawat and D. Schmidt, *Chem. Rev.*, 2016, **116**, 962-1052.
32. D. Gosztola, M. P. Niemczyk, W. Svec, A. S. Lukas and M. R. Wasielewski, *J. Phys. Chem. A*, 2000, **104**, 6545-6551.
33. T. Shida and S. Iwata, *J. Am. Chem. Soc.*, 1973, **95**, 3473-3483.
34. D. Markovitsi, I. Lecuyer and J. Simon, *J. Phys. Chem.*, 1991, **95**, 3620-3626.
35. R. J. Hudson, D. M. Huang and T. W. Kee, *J. Phys. Chem. C*, 2020, **124**, 23541-23550.
36. P. Borowicz and B. Nickel, *Opto-Electron. Rev.*, 2004, **12**, 22. 325-332.

37. J. Chen, S. Li, F. Gong, Z. Yang, S. Wang, H. Xu, Y. Li, J. S. Ma and G. Yang, *J. Phys. Chem. C*, 2009, **113**, 11943-11951.
38. S. R. Yost, E. Hontz, S. Yeganeh and T. Van Voorhis, *J. Phys. Chem. C*, 2012, **116**, 17369-17377.
39. D. Haarer, M. R. Philpott and H. Morawitz, *J. Chem. Phys.*, 1975, **63**, 5238-5245.
40. J. Zhang, H. Geng, T. S. Virk, Y. Zhao, J. Tan, C.-A. Di, W. Xu, K. Singh, W. Hu, Z. Shuai, Y. Liu and D. Zhu, *Adv. Mater.*, 2012, **24**, 2603-2607.
41. Y. Qin, C. Cheng, H. Geng, C. Wang, W. Hu, W. Xu, Z. Shuai and D. Zhu, *Phys. Chem. Chem. Phys.*, 2016, **18**, 14094-14103.
42. D. Vermeulen, L. Y. Zhu, K. P. Goetz, P. Hu, H. Jiang, C. S. Day, O. D. Jurchescu, V. Coropceanu, C. Kloc and L. E. McNeil, *J. Phys. Chem. C*, 2014, **118**, 24688-24696.
43. A. Fonari, C. Sutton, J.-L. Brédas and V. Coropceanu, *Phys. Rev. B*, 2014, **90**, 165205.
44. T. M. Wilson, M. J. Tauber and M. R. Wasielewski, *J. Am. Chem. Soc.*, 2009, **131**, 8952-8957.
45. G. Zhang, X.-K. Chen, J. Xiao, P. C. Y. Chow, M. Ren, G. Kupgan, X. Jiao, C. C. S. Chan, X. Du, R. Xia, Z. Chen, J. Yuan, Y. Zhang, S. Zhang, Y. Liu, Y. Zou, H. Yan, K. S. Wong, V. Coropceanu, N. Li, C. J. Brabec, J.-L. Bredas, H.-L. Yip and Y. Cao, *Nat. Commun.*, 2020, **11**, 3943.